Lawrence Berkeley National Laboratory
Recent Work

Title
SOME APPLICATIONS AT BERKELEY, AND POSSIBLE FUTURE TRENDS OF HIGH-VOLTAGE TRANSMISSION ELECTRON MICROSCOPY

Permalink
https://escholarship.org/uc/item/9fq9t0bj

Author
Thomas, Gareth.

Publication Date
1974

eScholarship.org
Powered by the California Digital Library
University of California

Chapter in "Physical Aspects of Electron Microscopy and Microbeam Analysis," Dr. B. Siegel and Dr. D. R. Beaman, eds., John Wiley + Sons

LBL-2274
c.1

SOME APPLICATIONS AT BERKELEY, AND POSSIBLE FUTURE TRENDS OF HIGH-VOLTAGE TRANSMISSION ELECTRON MICROSCOPY

Gareth Thomas

January 1974

Prepared for the U. S. Energy Research and Development Administration under Contract W-7405-ENG-48

For Reference

Not to be taken from this room

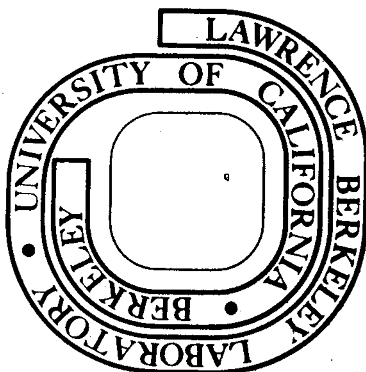

LBL-2274
c.1

DISCLAIMER

This document was prepared as an account of work sponsored by the United States Government. While this document is believed to contain correct information, neither the United States Government nor any agency thereof, nor the Regents of the University of California, nor any of their employees, makes any warranty, express or implied, or assumes any legal responsibility for the accuracy, completeness, or usefulness of any information, apparatus, product, or process disclosed, or represents that its use would not infringe privately owned rights. Reference herein to any specific commercial product, process, or service by its trade name, trademark, manufacturer, or otherwise, does not necessarily constitute or imply its endorsement, recommendation, or favoring by the United States Government or any agency thereof, or the Regents of the University of California. The views and opinions of authors expressed herein do not nccessarily state or reflect those of the United States Government or any agency thereof or the Regents of the University of California.

Offprints From:
PHYSICAL ASPECTS OF ELECTRON MICROSCOPY
AND MICROBEAM ANALYSIS
Edited By Dr. Benjamin Siegel and Dr. D. R. Beaman
Published By John Wiley & Sons, Copyright 1975

CHAPTER 6

Some Applications at Berkeley, and Possible Future Trends of High-Voltage Transmission Electron Microscopy

GARETH THOMAS

INTRODUCTION

High-voltage electron microscopy (HVEM) has now become established in materials science and is slowly but surely being recognized for biological applications. This is evident from the recent installations of 1 MeV instruments in several laboratories in the United States and elsewhere. The main reasons for utilizing high voltages and a summary of applications are given in Table 1.

Electron microscopy is an essential tool for characterizing the structure of materials, and considerable progress has been made in metallurgy over the past 20 years. Developments are less advanced in the case of engineering ceramic materials, partly because they are more complex and because they are difficult to prepare suitably thin for transmission electron microscopy. Similarly, many organic solids of interest cannot be studied easily because of the problem of radiation damage which causes specimen destruction through such processes as bond breaking, ionization, and cross-linking. In these latter cases the high-voltage electron microscope is particularly important because (1) the greater penetration enables thicker specimens to be examined, thereby minimizing specimen preparation difficulties, and (2) there is a reduction in radiation damage with increasing energy. However, at certain threshold energies, knock-on damage occurs in which atoms are ejected from their lattice sites. In metals, this effect is one of major importance because (1) such damage can be studied directly in the microscope, hence it is a powerful technique for understanding problems of major interest in reactor technology (e.g., swelling), especially in view of the energy crisis and the need for safe application of nuclear reactors; and (2) knock-on damage modifies the microstructure and from this viewpoint determines the maximum operating voltage. Some other disadvantages, notably the high cost of high-voltage electron microscopes, are listed in Table 2.

Some examples of current research using the Berkeley 650 kV electron microscope are presented in this chapter, and no attempt is made to provide a comprehensive review of the field. Surveys of our work have also been made in several conferences (e.g., Refs. 1–3) and abstracted in the 1973 EMSA Conference publication [4].

Table 1. Some main advantages of high-voltage transmission electron microscopy

1. Penetration
    - Light materials $\simeq$ 14 μm at 2.5 MeV
    - Medium-heavy $\simeq$ 2–3 μm at 1 MeV (maximum kV for routine microscopy)
    - Applications include:
        - Biological systems-natural environments, thick sections
        - Ceramics, minerals, difficult to thin materials
        - Nondestructive, precious samples, e.g., moon dust
        - Particle analysis (extractive metallurgy), pollution research
        - Heavy elements
        - Semiconductor devices
        - Crystals of low defect densities
        - Better statistics-larger sampling (stereomicroscopy)
        - *In-situ* studies (dynamic events), environmental; gases, liquids, etc.
        - Interfaces, e.g., diffusion gradients, semiconductors, multiphase systems
2. Resolution Increase
    - Chromatic and spherical aberrations
    - Reduced area for selected area diffraction
    - Lattice defects
3. Special Diffraction Effects—Crystals
    - Channelling increased transmission
    - Critical voltage effect
    - Contrast: Improved magnetic contrast
        - Improved resolution of lattice defects (bright field imaging using high order systematics)
4. Displacement Damage
    - Simulates nuclear reactors, e.g., at 1 MeV point defect damage in Fe in electron microscope in 1 min $\equiv$ 450 days in reactor
    - Maximum voltage should be about 1.5 MeV (1.25 MeV is threshold for uranium)
5. Ionization Damage
    - Decreases with increasing kV (e.g., beam-sensitive materials—biological, polymers, ionic crystals, etc.
6. Superior Vacuum
    - Lower contamination rate
7. Higher Brightness

PENETRATION, DAMAGE, AND OPTIMUM VOLTAGES

It is difficult to define penetration satisfactorily for all applications. Measurements up to 2.5 MeV have been made recently on inorganic materials based upon determination of the penetrable thicknesses for a given absorption limit as evidenced by damping out of fringes at planar faults extending through the specimen [5,6]. The results are given in Fig. 1 and indicate that although the penetration to 2.5 MeV is considerable for light elements, there does not appear to be much benefit above

Table 2. Some disadvantages of high-voltage transmission electron microscopy

1. High cost and maintenance (capital costs are $\simeq 10^6$ dollars for 1.2 MeV microscopes).
2. X-ray hazard (can be avoided by careful screening, but needs monitoring).
3. Radiation Damage to Specimens
   Knock-on damage in crystals destroys substructure, limits maximum kV usable, therefore, limits penetration advantages.
4. Manufacturing Defects
   Need for better, high quality commerical specimen stages, e.g., goniometer stage for range of temperatures and environments.

1 MeV for medium (and heavy) atomic weight materials. However, since the threshold voltage for knock-on displacement damage increases with increasing atomic number, microscopes should have a voltage range capable of producing damage for a wide range of materials. Since this voltage is about 1.2 MeV for uranium, it is suggested that a useful upper limit should be about 1.3 to 1.5 MeV (to allow some leeway and also for adequate conditioning). As shown in Fig. 2, radiation damage quickly obscures features of interest (in this case a stacking fault) so that for nonradiation damage studies, the limiting voltage is determined by the

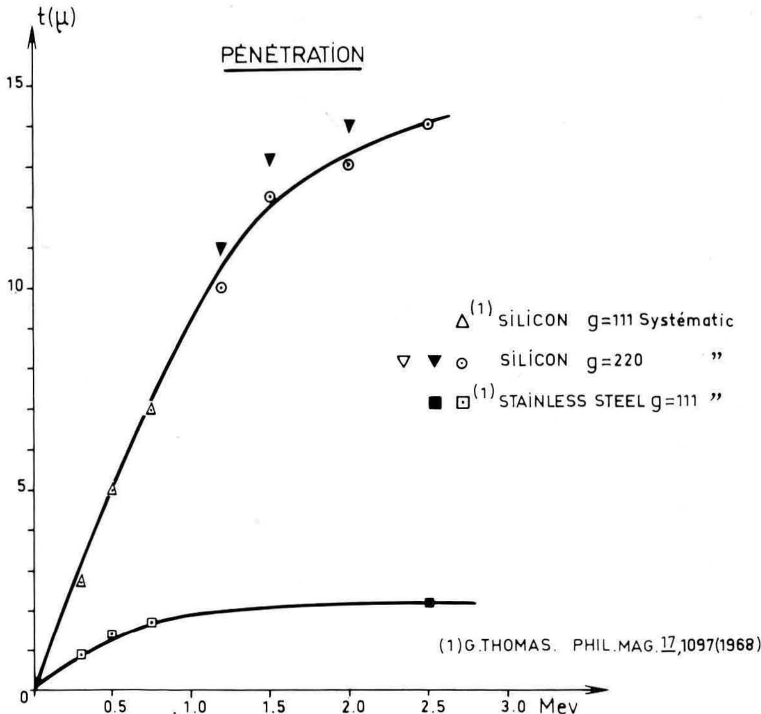

Figure 1. Penetration measurements made on the Toulouse 3 MeV microscope for Si and austenitic stainless steel [6].

Figure 2. Intense knock-on radiation damage in Cu–14 at. % Al alloy after 1 hr exposure at 1 MeV (observations from 1 MeV instrument, Nagoya University, Japan); the stacking fault arrowed is barely visible.

threshold for knock-on damage. Some examples of these voltages are given in Table 3.

The optimum voltages for organic solids are not yet well established. Preliminary results on crystalline amino acids (Glaeser and Thomas to be published; see also Chapter 12) indicate that the reduction in bond-breaking damage (as determined by the destruction of crystallinity from diffraction patterns during exposure in the electron beam) seems to obey laws of stopping power with some exceptions, indicating that from this viewpoint, 1 MeV is optimum. At higher voltages advantages are to be expected from increased penetration (Fig. 1) and resolution, principally due to the reduction in chromatic and spherical aberrations. More experiments require voltages above 1 MeV, and this will mean more research on the Toulouse and Osaka 3 MeV instruments.

EXAMPLES OF APPLICATIONS UTILIZING INCREASED PENETRATION

Introduction

The examination of nonmetallic materials is proceeding rapidly at this time, especially at high voltages. This is due to the greater penetration and reduced ionization damage at high voltages, coupled with considerable improvements in specimen preparation techniques such as ion thinning or sputter-etching. It is interesting that the latter techniques were first tried 20 years ago when transmission electron microscopy of crystals was just emerging, but due to the success of chemical and electrochemical thinning techniques, especially for metals, ion thinning was not utilized until fairly recently when nonmetallic solids started to be examined in detail.

Ion Thinning

The principles of the latest developments in ion-thinning have been described by Barber [7]. A schematic diagram of the apparatus in use at Berkeley which is a

Table 3. Some examples of threshold electron energies for atomic displacements

Metal	Z	Displacement energy, eV	Electron energy, kV
Ti	22	29	440
Fe	26	24	430
Ni	28	24	450
Cu	29	24	500
Mo	42	37	870
W	74	35	>1000
Au	79	34	>1000

modification of a commercial sputtering device, is shown in Fig. 3. We are grateful to Professor J. M. Christie (U.C.L.A.) for assistance in this modification.

When preparing thin foils, it is important to keep their temperature sufficiently low to avoid structural changes. Consequently, ion current densities in excess of $\simeq 200\ \mu A/cm^2$ are unnecessary. This is a factor of 10^1 to 10^2 lower than the ion density in normal sputtering systems. Moreover, if the ion energy is increased beyond $\simeq 10$ keV, most of the increase is dissipated in deeper penetration (which is clearly undesirable) and not in greater efficiency of sputtering. With care, damage to the surfaces by ion bombardment can be kept to a minimum. However, ion damage in the electron microscope can occur (discussed later). The ion guns are of the hollow anode type and each produces one beam. Each anode is connected through a large ballast resistor to a well-stabilized 10 kV, 10 mA dc supply. The bombardment chamber is mounted over a 6-in. diffusion pump and liquid nitrogen trap, backed by a two-stage rotary pump. The vacuum system maintains a working vacuum of between 10^{-3} and 10^{-4} torr while high purity argon gas is entering the anode–cathode interspace through fine needle valves. The main disadvantage of the cold cathode ion source is that it necessitates a relatively large flow of gas into the system. With a typical gas flow rate of $\simeq 5 \times 10^{-2}$ torr/liter-sec, there is an ion current of about 70 μA per gun at 6 kV. The ion current density at the sample is about 200 $\mu A/cm^2$. The ion currents can be measured and balanced by means of retractable probes.

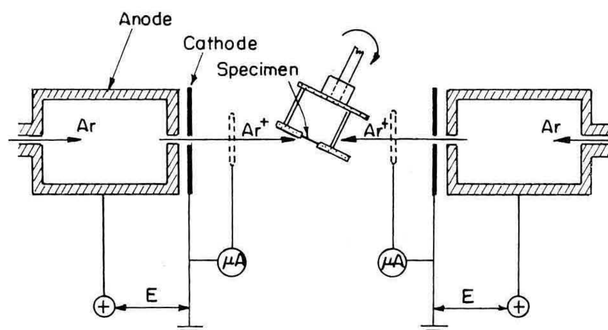

Figure 3. Schematic diagram of ion-beam thinning device (see text).

The sample, with its periphery sandwiched in a thin stainless steel holder, is rotated in the ion beams. The inclination of its exposed surfaces with respect to the beams can be pre-set at angles between 0 and 30°. It is important that the ion beams should "see" both surfaces and erode them at equal rates if no provision is made to stop the back-diffusion of sputtered atoms from the sample and its holder. To minimize the redeposition of sputtered material on the sample, one can place a partial shield around it which is cooled by liquid nitrogen. The shield also prevents the occurrence of arc discharges in the ion guns when thinning materials which give off voltatile constituents. Eventually, the ion sources become electrically unstable to glow discharge because of enlargement of the holes in the cathodes. In normal use, however, they have a life of about 250 hr. Some ionization damage occurs to the specimen as evidenced by formation of defects such as dislocation loops near the surfaces of the foil (see Fig. 6).

DeJonghe and Thomas [8] have also observed that ion damage in the form of vacancy defects occurred during observation of cobalt ferrite foils in the 650-kV microscope. Mass spectrometer measurements of the impurities in the objective chamber indicate that nitrogen and oxygen ions are the most likely ones to cause damage. The density of defects does not seem to exceed about $2 \times 10^9/cm^2$, and therefore do not mask other features. Nevertheless, their presence must be recognized as arising "artificially," i.e., they are not characteristic of the normal microstructures. They can be seen as small strain contrast defects in Figs. 7 and 8.

Examples of Research on Spinels

Presently, about 30 different cations are known to form spinels with oxygen. We are studying cobalt and lithium ferrites which are ferrimagnetic and are thus of interest in the electronics industries. Conventionally, grain size or porosity has been used to control the magnetic properties of polycrystalline ferrites, but it is likely that heat treatments, producing the proper microstructure, could lead to magnetic materials with highly desirable properties. Compared to mechanical properties, the field of microstructural relationships with magnetic properties has hardly been explored. Our results of phase transformation studies in cobalt ferrites over the composition range Co/Fe = 0.54/0.76 have been published previously [9].

The structure of spinels is best understood if attention is focused on the oxygen sublattice. The oxygen sublattice is face-centered cubic. The octahedral and tetrahedral interstices are partially filled with the cations cobalt (or lithium) and iron. These ferrites are inverse spinels, which means that the trivalent ions prefer the tetrahedral sites rather than the regular octahedral sites. Lithium ferrites in the composition range being studied, viz., $LiFe_5O_8$, order below 750°C.

Except for simple structures, dislocations in oxide crystals have been somewhat neglected by the ceramist, mainly because most highly ionic crystals are very brittle, even up to high temperatures. The efforts in studies of mechanical properties of ceramics have therefore been concentrated on crack formation and propagation on a macroscopic scale. Dislocations play a fundamental role in the mechnical behavior of oxide materials, as they do in metals, and the details of the dislocation structure itself should be of great importance with regard to high temperature deformation, fracture, or creep. Detailed contrast experiments have therefore been carried out to determine the degree of dissociation of dislocations in cobalt ferrite spinels (see Ref. 3).

The geometry of dislocation dissociation in the spinel lattice has been discussed in detail by Hornstra [10], who advanced arguments for a fourfold dissociation of a perfect dislocation in spinels. The main arguments are that local electroneutrality can only be maintained in the fourfold dissociated configuration and that, in nature, spinels are found that are twinned on {111} planes. This observation of twinning in natural spinels was seen as evidence for the presence of Shockley partials. For twofold dissociation, the bounding partials have identical Burgers vectors both equal to $a/4\langle 110\rangle$. They are bounding a stacking fault in the cation sublattice only, since the fcc oxygen sublattice actually has half the lattice parameter of the spinel lattice. Twofold dissociation on {100} planes was observed in magnesium aluminate spines, and the nature of the cation stacking fault has been discussed by Lewis [11]. For the fourfold dissociation the two outer pairs of Schockley partials bound a compound fault: an intrinsic stacking fault in the oxygen sublattice plus a fault in the cation sublattice. In this fault the cations would have moved to their favored crystal coordination.

Defects in Lithium Ferrite

Lithium ferrite undergoes an order–disorder transformation at about 750°C and so the nature of the defects depends on the state of order.

Disordered $LiFe_5O_8$

Flux-grown crystals of $LiFe_5O_8$, quenched from a temperature above the ordering temperature, contained areas with a high density of defects (Fig. 4). A $\mathbf{g}\cdot\mathbf{R}$ analysis on these faults showed that $\mathbf{R} = \frac{1}{4}\langle 110\rangle$.* The predominant fault plane is {110} with **R** always perpendicular to the fault plane. However, a few isolated examples of {112} and {123} fault planes were also found.

Ordered $LiFe_5o_8$

From an analysis of the ordered structure, it could be predicted that in the ordered state, antiphase boundaries (APBs) with $\mathbf{R} = \frac{1}{2}\langle 110\rangle$, would be formed. Contrast analyses are in agreement with this prediction [12]. An example of APBs is shown in Fig. 5.

Antiphase boundaries can end on a dislocation with $b = \frac{1}{2}\langle 110\rangle$ as shown in Fig. 6. In Fig. 6*a*, taken in a superlattice reflection, a $\frac{1}{2}[110]$ APB terminating at a dislocation $b = \frac{1}{2}[110]$ is seen. The plate was taken with $w_{022} = 0$ (w is the deviation parameter from the exact Bragg condition). Due to the interaction between the 011 superlattice beam and the 022 beam, the APB is visible in the 022 dark field, although $\alpha = 2\pi\mathbf{g}\cdot\mathbf{R} = 2n\pi = 0$. The dislocation confining the APB is split into two partials with $\mathbf{b} = \frac{1}{4}\langle 110\rangle$ with a cation stacking fault in between, Fig. 6*b*. Figure 6*c* was taken with $w_{066} = 0$. The two faults are out of contrast now and the two partials are sharply resolved. As discussed in the section on Many-Beam, Dynamical Diffraction Effects, an advantage of using high order bright field images at high voltages is the improvement in resolution of dislocation images. The images become narrower as $n\mathbf{g}$ is increased. This phenomenon is clearly seen in Fig 6*c* where the image widths are < 50 Å.

*$\mathbf{g}$ is the reciprocal lattice vector of the operating reflection and **R** is the displacement vector of the defect; $\mathbf{g}\cdot\mathbf{R}$ analysis refers to the well-known visibility criteria for defects in crystals.

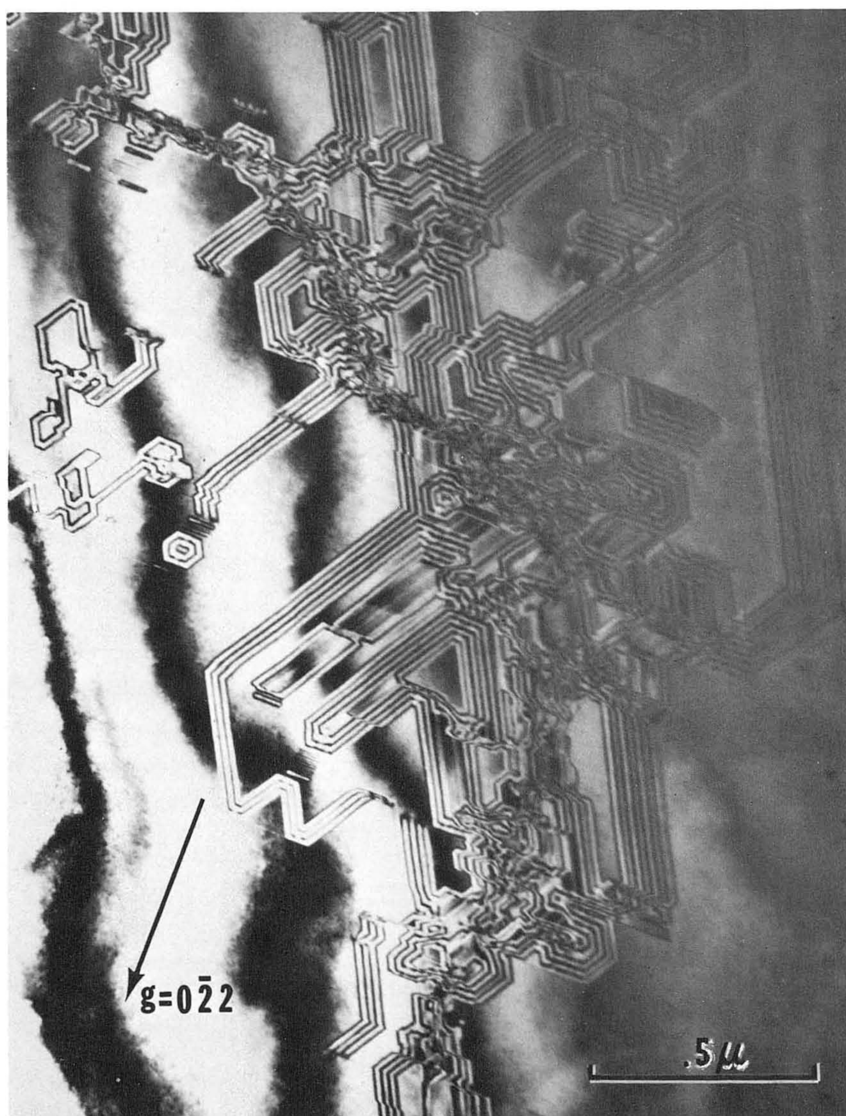

Figure 4. Disordered $LiFe_5O_8$ showing {110} cation stacking faults (courtesy Van der Biest [12]).

Magnetic Domains in Cobalt Ferrite

Cobalt ferrites are ferrimagnetic oxides of the spinel type, exhibiting magnetic ordering along ⟨100⟩. Ferrimagnetic domain walls have been observed in this ceramic material with the specimens in the regular position [13]. Even though the field of the objective lens is quite high (~7 kG), domain walls may be observed if the specimens are symmetrically oriented with respect to the field direction of the objective lens, so that adjacent domains have approximately equal energy. Such orientations for cobalt ferrites are ⟨111⟩. Under these conditions, only $\pi/2$ domain walls are expected. Such $\pi/2$ ferrimagnetic domain walls are shown in Fig. 7. Since magnetostriction accompanies magnetic ordering, the domain wall boundaries

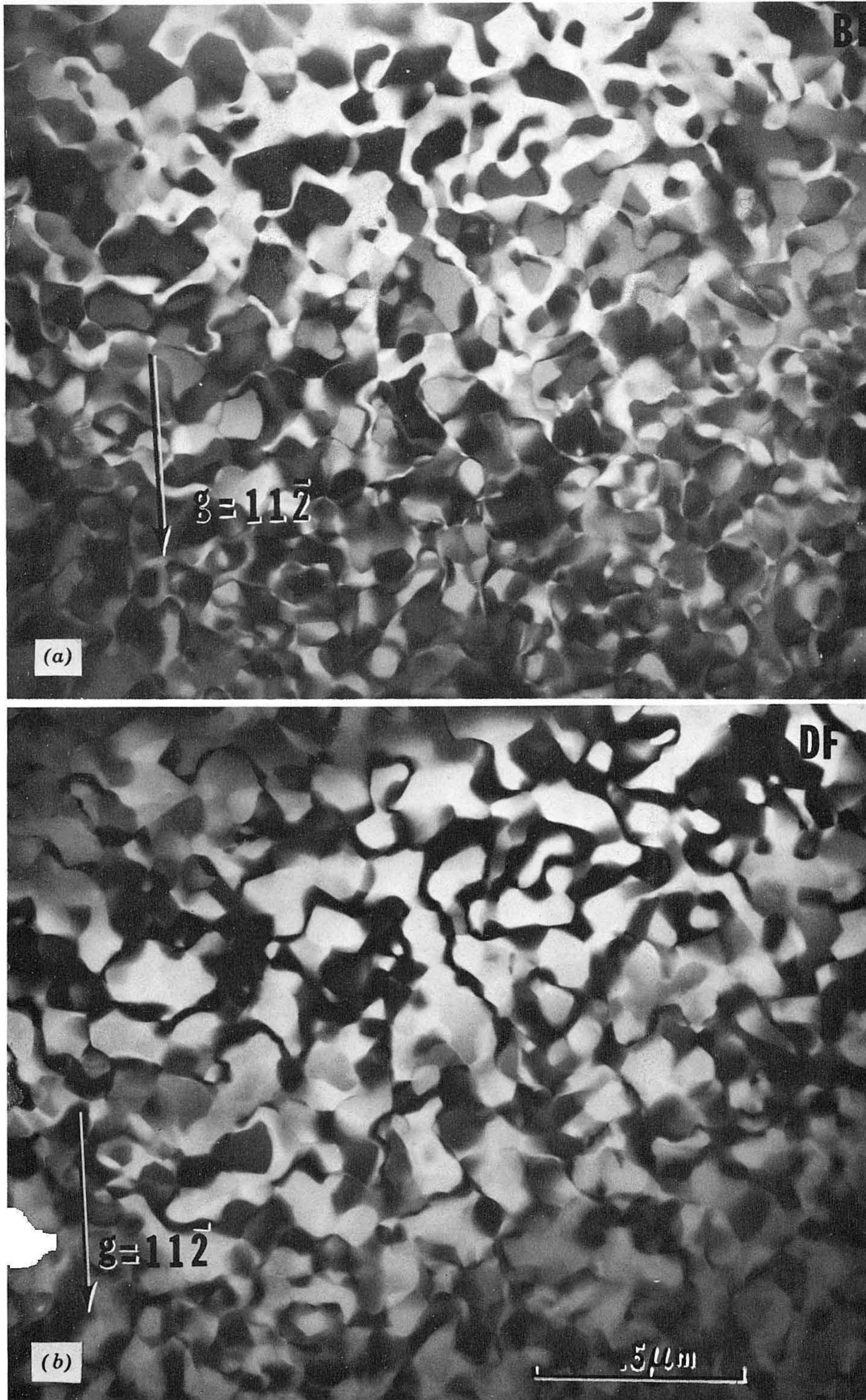

Figure 5. Examples of bright- and dark-field images of APBs in order $LiFe_5O_8$ (courtesy Van der Biest).

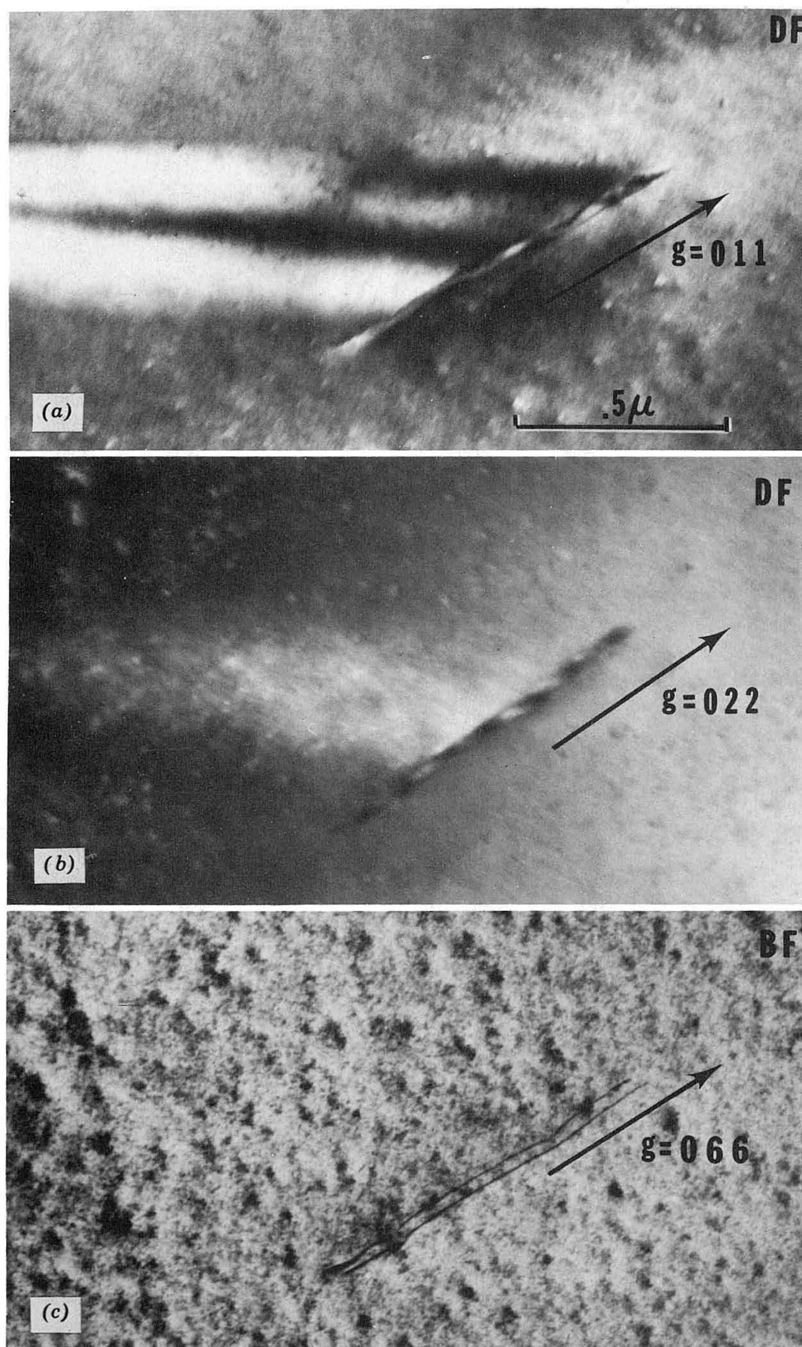

Figure 6. Contrast experiments on fully ordered $LiFe_8O_8$. (*a*) 011 superlattice dark-field image. (*b*) 022 fundamental dark-field image (cation fault visible). (*c*) 066 bright field resolving partials. The background structure is due to ion damage during specimen thinning (courtesy O. van der Biest [12]).

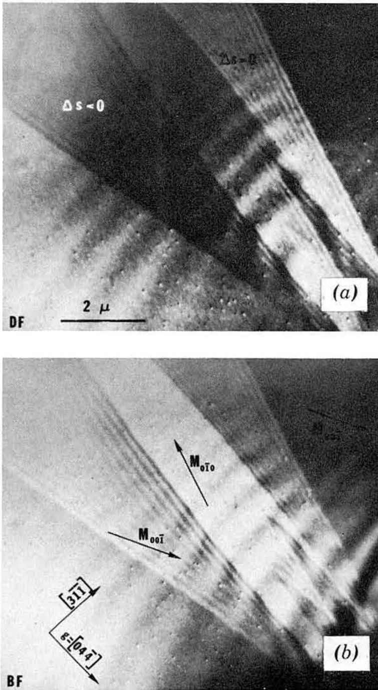

Figure 7. Dark- and bright-field images of ferrimagnetic domain walls (90° Bloch Walls) in $CoFe_2O_4$. The orientation is <111> with $g = 044$. The direction of magnetization M is indicated (courtesy De Jonghe [13]).

are also coherent twin boundaries which can be imaged with the specimen in focus. The fringe contrast (δ-fringes) is then due to a slight change in the sign of s across the boundary. This is quite analogous to observations on NiO reported by Ramaut et al. [14].

The $\pi/2$ ferrimagnetic domain walls were observed to lie mainly on 110 planes, though deviations are possible. Such deviations are shown in Fig. 8. The magnetic changes that must exist at the curved sections of these walls did not noticeably influence the fringe contrast. The small defects visible in this micrograph are a result of ion radiation damage during observation in the high-voltage microscope.

Domain walls can be made to move easily by slightly tilting the specimen away from the exact ⟨111⟩ orientations. Zigzag configurations were often observed, and in those cases the domain wall displacements were nearly perpendicular to the direction of domain growth.

Particulates

The increased penetration capabilities permit HVEM to be utilized in studies of particulate materials. In fact, current research programs involve characterizing particulate materials ranging from those at the depth of the ocean floor, through pollutants in the earth's atmosphere, to dusts and rocks collected from the surface of the moon—truly universal applications. Here, brief mention is made of a promising, though tedious, program of analyzing particulates in ocean floor manganese nodules for possible useful raw materials suitable for mineral processing and eventual metal extraction. It is estimated that at least 10^{11} tons of nodules exist on the Pacific Ocean bed alone, so there is considerable interest in these materials.

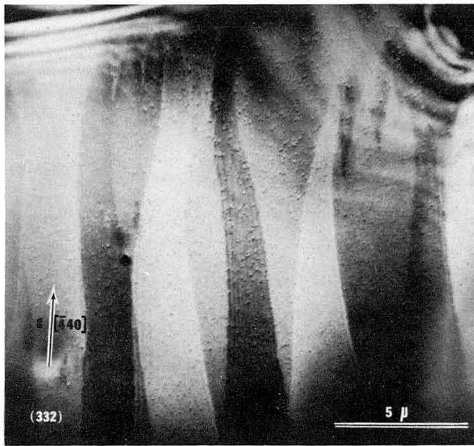

Figure 8. Curved domain walls in $CoFe_2O_4$ (courtesy De Jonghe [13]).

The main conclusions from selected area diffraction analyses [2,15] is that most particles in the size range 100–540 Å, of the nodules so far examined contain ferric hydroxide. Mineral identification from accurate *d*-spacing measurements, such as analysis of asbestos fibers which are too thick ($\simeq 2$ μm) for identification at 100 kV [16] is facilitated by computer programs that are also used in environmental research. HVEM also allows these fibers to be examined for longer times because of the reduction in ionization damage at higher energies.

Mineralogy

Many examples of the application of HVEM to minerals are now appearing in the literature. At Berkeley, we have a cooperative program between Geology and Materials Science. One of the projects is concerned with a study of ordered structures and APBs in feldspars, especially anorthite [17], $CaAl_2Si_2O_8$. Anorthite crystallizes in the space group $P\bar{1}$. It has a primitive unit cell, and the *c*-axis (14 Å) is about twice that of the feldspars albite or microcline [18,19].

The X-ray reflections of anorthite have been classified as type *a* ($h + k$ even, l even), *b* ($h + k$ odd, l odd), *c* ($h + k$ even, l odd), and *d* ($h + k$ odd, l even). Type *a*-reflections are the only reflections present in alkali feldspars; *b*-reflections have been attributed to Si-Al order and are also present in bytownites (An 80 to 90). They become increasingly weak with decreasing An-contents and split up (*e*-reflections in intermediate plagioclase). The crystal structure with only *a*- and *b*-reflections has been called body-centered anorthite. Anorthite with sharp *c*- (and the much weaker *d*-) reflections is called primitive anorthite, and that with diffuse *c*-reflections transitional anorthite. The boundaries between these types of structure are gradational.

Type *b*-APBs occurring in calcic plagioclases from lunar basalts were first observed by Christie et al. [20]. These authors report that APBs were in contrast using *b*-reflections and out of contrast with *a*- and *c*-reflections. They attribute the *b*-APBs to subsolidus ordering of Si-Al and conclude that the antiphase vector is ½ [001]. If this were the case, the *b*-APBs should be observable also in *c*-reflections, because both *b*- and *c*-reflections would give $\alpha = \pm\pi \bmod 2\pi$ for $R = \frac{1}{2}[001]$. In

a later paper, Heuer et al. [21] attribute the failure to image *b*-APBs with *c*-reflections to their weakness and diffuseness.

More recently, we have found in an anorthite crystal (An 92.5) from lunar breccia 15459, 0.05 mm in diameter, the existence of both type *b*- and type *c*-APBs, the *c*-reflections being relatively intense and sharp. This is illustrated in Fig. 9 where both *b* and *c*-APBs are simultaneously imaged. By tilting, the appropriate contours can be swept across the field of view showing both types of APBs coexist in the same area. Using the visibility criterion for phase contrast, it was concluded that the APB displacement vectors are ½ [110] for *b*-APBs and ½ [111] for *c*-APBs.

In order to estimate the contrast to be expected for the various APBs in multiple-beam situations, a computer program capable of calculating the results of such interactions was specially modified to handle the treatment of a triclinic unit cell with a large number of atoms and a variety of species as described by Müller et al. [17]. The results are shown in Fig. 10.

An APB would not normally be expected to be detectable with an *a*-reflection such as for $g = 22\bar{2}$ even though the boundary is in strong contrast for the first-order image ($g = 11\bar{1}$), Fig. 11. This is so because the phase angle for the second-order reflection is 2π rad (i.e., $\mathbf{g}\cdot\mathbf{R} = 1$). However, under strong multiple-beam conditions wherein systematic or simultaneous reflections are unavoidable, the unexpected image would appear by double diffraction (i.e., dynamic interaction with other diffracted beams). Hence, Fig. 10 also shows the fairly strong dark-field profile for an APB in the $22\bar{2}$ image. This profile is asymmetric since strong anomalous absorption effects are associated with this reflection. This result has been confirmed experimentally [17].

Although the computer profiles of Fig. 10 are shown for a foil thickness of only two extinction distances, which may seem to be small, it must be remembered that extinction distances for reflections capable of detecting APBs in anorthites are generally quite large. For the $11\bar{1}$ reflection at 650 kV the extinction distance ξg is 5950 Å (computer calculated for relativistic electron scattering from anorthite) and the foil thickness for an image with a similar number of APB fringes would be 1.2 μm, which is a thick foil.

Figure 9. Dark-field image of lunar breccia 15459 in which simultaneous excitation of *b*-type ($21\bar{3}$) and *c*-type ($20\bar{3}$) diffraction occurs. At these extinction contours *b*-type APBs (right) and *c*-type APBs (left), respectively, are imaged.

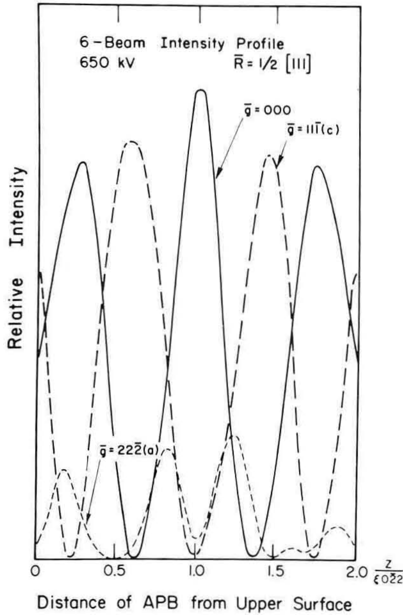

Figure 10. Computed 6-beam intensity profiles for c-type APBs in anorthite; profiles for bright-field ($g = 000$) and $11\bar{1}$ (c-type) and $22\bar{2}$ (a-type) dark-field images. Foil normal [314] 650 kV [17].

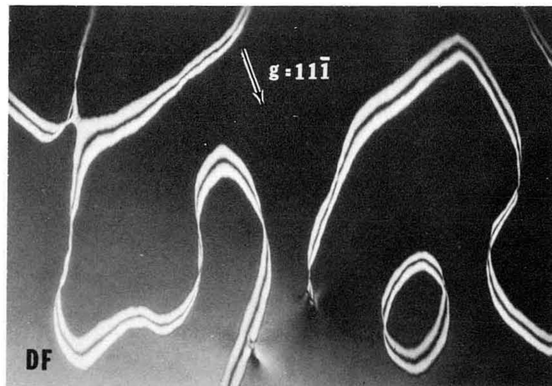

Figure 11. Strong c-type APB contrast in anorthite; typical π fringe contrast dark field in $11\bar{1}$ [17].

MANY-BEAM, DYNAMICAL DIFFRACTION EFFECTS

Contrast and Resolution

As the electron energy increases, more and more reflections are excited in crystals and two-beam dynamical theory is no longer adequate. Some interesting properties can occur due to many beam effects and which have useful practical applications. Here, mention is made only of some effects associated with systematic reflections, i.e., many excitations occurring along one reciprocal lattice direction but none (or weak) reflections are excited along other directions simultaneously.

We have shown earlier the advantages of bright-field and dark-field techniques utilizing high-order systematic reflections for improving resolution, e.g., Bell and

Thomas [1] and Goringe et al. [22]. Further work using 13-beam systematic computations and experimental observations [23] on several systems have provided some new results at 650 kV as shown in the corresponding Figs. 12*a–d*. Figures 12*c* and *d* resolve partials of about 75 Å spacing of the pure edge components of a shear loop (**b** $= a/2\,[011]$) in B-doped Si. This spacing is identical to that reported for 100 kV weak-beam analysis by Ray and Cockayne [25] for pure Si. Thus the stacking fault energy in the B-doped specimen is also $\simeq$55 ergs/cm^2. The experimental result, Fig. 12*c*, shows higher contrast of the weak-beam images at high voltages (compare to calculation of Fig. 12*a*).

For resolving closely spaced dipoles [23] the best conditions for imaging have been shown by calculation (9-beam systematic) and experiment to be near $2g$ (outside contrast) in bright field or the corresponding weak-beam dark field in $-g$. These conditions provide maximum image separation, best contrast, and only slightly wider images than if $ng > 2$.

Bell [24] first showed that bright-field images in $2\bar{g}$ of stacking faults were contrasty or not dependent on the sign of the phase change $\alpha = 2\bar{g}_1\pi \cdot R$ at the boundary (g_1 is the first order of the systematic set). Subsequently, many more calculations and images have been examined for faults in Si which whowed this effect depends on thickness (bright field, Fig. 13) and w. However, the dark-field image in g when $2g$ is satisfied (or slightly negative but not positive) is directly indicative of the sign of α independently of thickness (Figs. 13 and 14) being of better contrast when $\alpha = -2\pi/3$ (modulus 2π). Thus this dark-field image gives a rapid method for determining whether faults are intrinsic or extrincic, especially for loops etc. within the foil.

Critical Voltage Effect

This effect is now well known as being due to multiple-beam interactions. Of interest in HVEM is the critical voltage V_c for second-order reflections, i.e., the voltage at which the intensity of the second-order reflection becomes very small. This voltage is easily measured to accuracies of 2 to 5 kV experimentally and can be calculated [1,26–28]. Some values of V_c using 3-beam calculations are given in Table 4. It can be seen that microscopes of energies >1.5 MeV are necessary for measurements.

Table 4. V_c values using 3-beam calculations

Metal	Reflection	V_ckV
Al	222	430 kV
Ni	222	295 kV
	440	1870 kV
Fe	220	305 kV
	400	1300 kV
Si	440	1440 kV

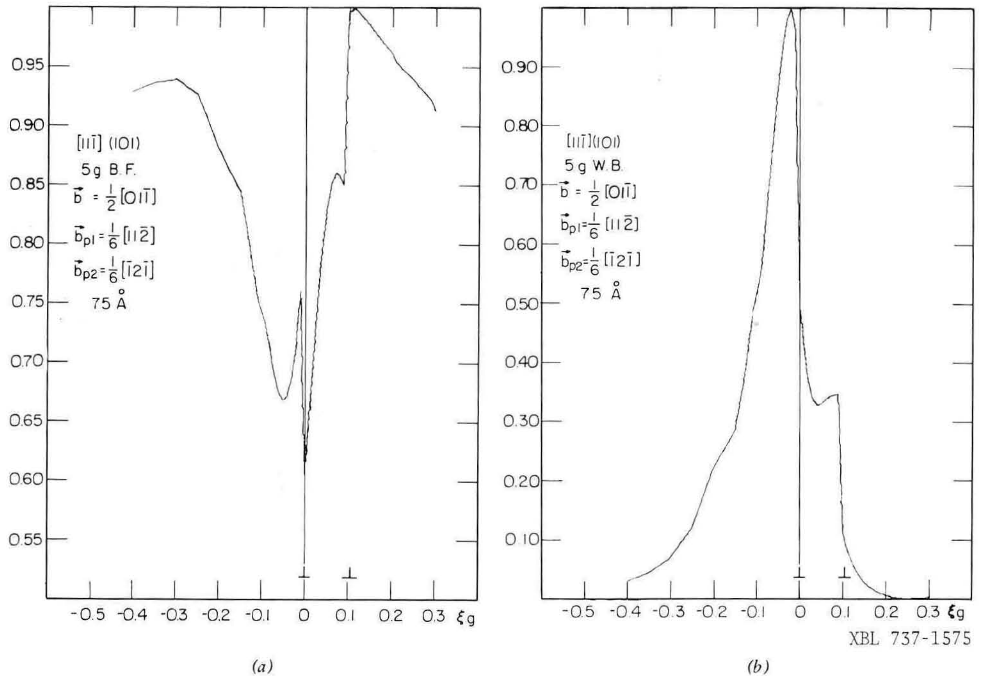

Figure 12. Computed images of partial dislocations for a dissociated edge dislocation **b** = ½ [101̄] in Si. (*a*) Weak-beam dark field. (*b*) Bright field with 555̄ satisfied. Dislocation at 2.5 ξg, thickness = 6 ξg (courtesy L. J. Chen).

For cubic crystals, the critical voltage is given by the following expression {three-beam theory; Bell, unpublished}:

$$V_c = 1605(h^2 + k^2 + l^2)\,\frac{a_0}{Fx} - 511 \tag{1}$$

where

a_0 = lattice parameter
$x = (fg/f2g)^2 - 1$
F = structure factor of 2nd order reflection
fg = scattering factor for reflection g

This shows that the critical voltage is very sensitive to the (local) structure factor and consequently varies with composition. Thus measurements of V_c can be useful for many applications, e.g., determination of scattering factors, Debye temperatures, degree of order, segregation [26], and precipitation [27,29]. However, for measuring compositional changes in localized regions, the difference in scattering factor must be large enough to change V_c measurably over short distances, i.e., within the spatial resolution ($\simeq$ 1000 Å). This limitation is set chiefly by spherical aberration. For example, V_c for Al {222} changes by only -6 kV per atomic % of silver, (note that for every 10°C rise in temperature, V_c drops 5 kV for {222} in Al [26] so temperature has a strong effect and local beam heating should be avoided).

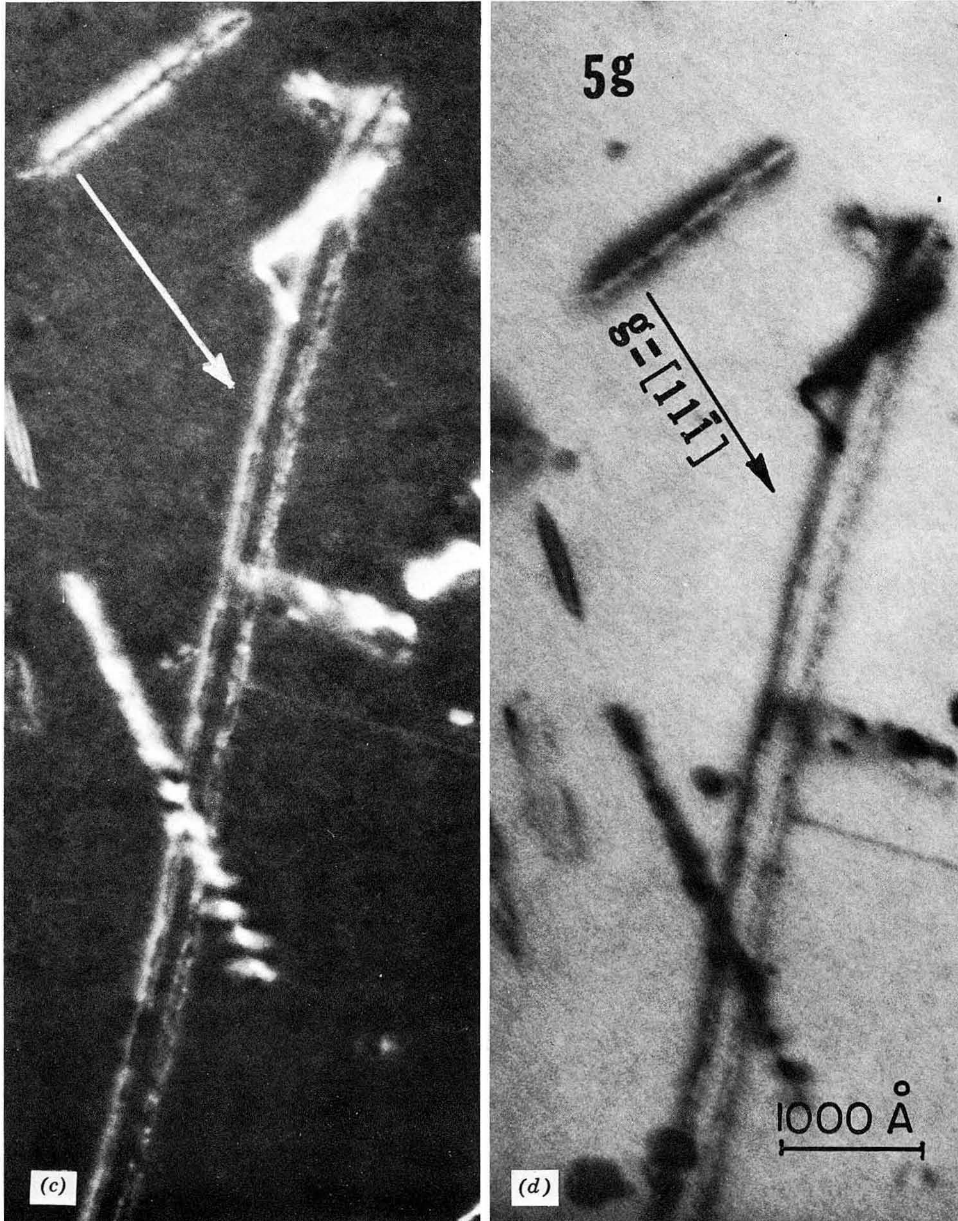

Figure 12. Examples corresponding to Figure 12 a and b. (*c*) Weak-beam dark field. (*d*) Bright field with $55\bar{5}$ satisfied, partials are resolved at edge components of elongated prismatic loop in B-doped Si.

A recent paper by Butler [29] discusses the present limitations of using V_c for studies of compositional gradients and precipitation in alloys (see Chapter 8). Present applications at Berkeley include studies of short-range order and contrast effects.

Equation 1 indicates that local disturbances in lattice constant a_0 will also modify V_c and high contrast will be obtained at defects such as dislocations [1]. An example, {440} Si, for which V_c was measured to be 1.4 MeV [6] is shown in Fig. 15

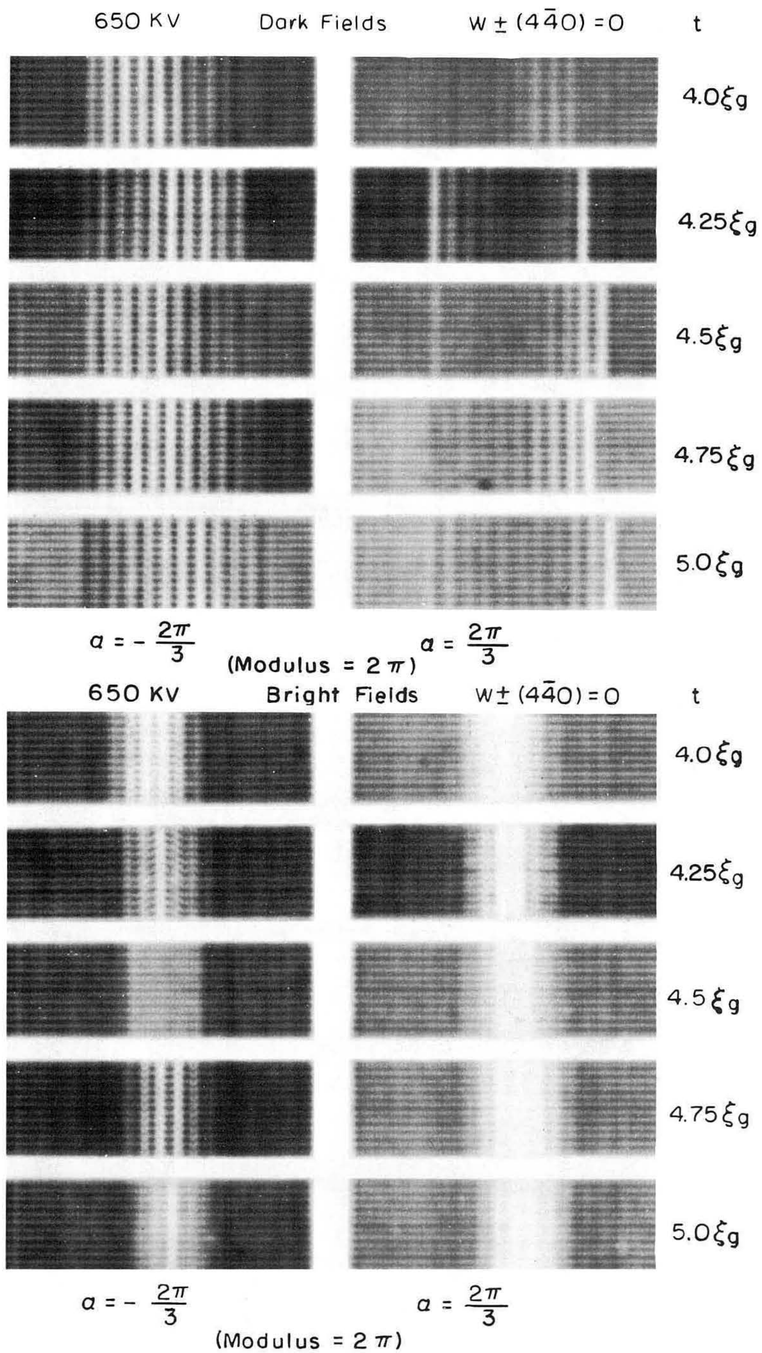

Figure 13. Computer simulated images of stacking faults in silicon (courtesy L. J. Chen).

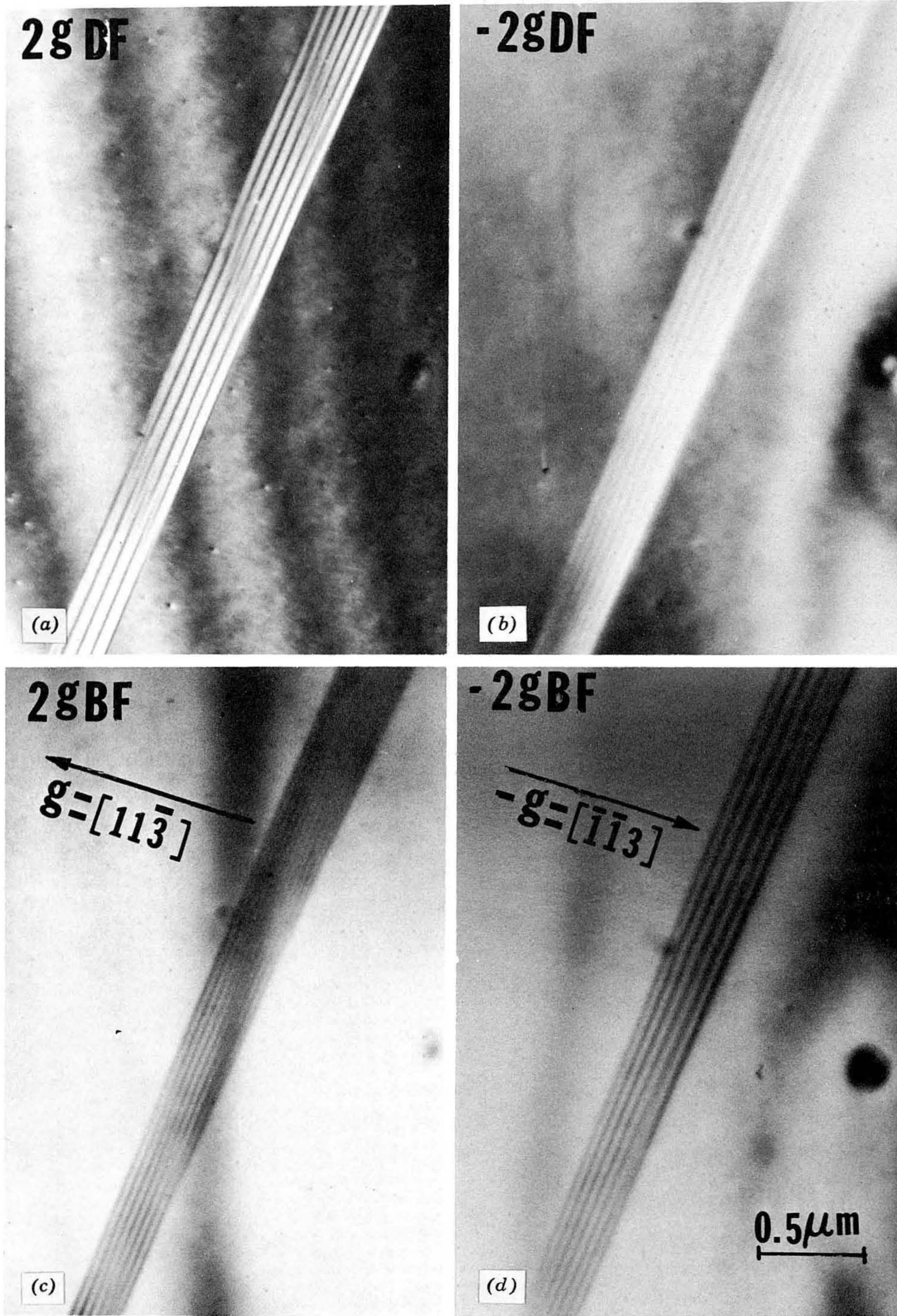

Figure 14. Experimental examples corresponding to Fig. 13; notice that contrast in bright field depends on thickness whereas in dark field it depends only on the sign of α (courtesy L. J. Chen).

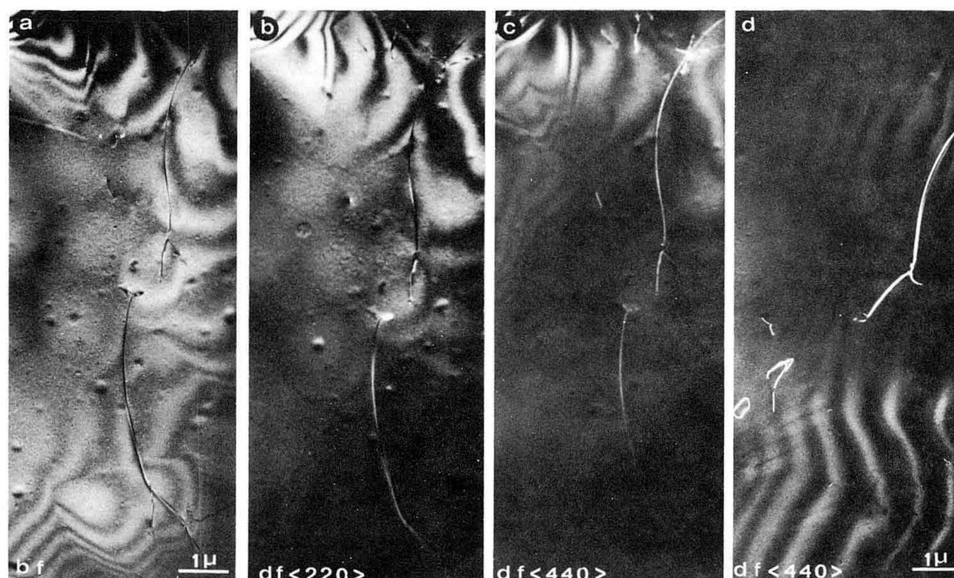

Figure 15. Images of dislocations in Si at 1.4 MeV (taken on the Toulouse 3 MeV microscope): (*a*) bright field, (*b*) dark-field first-order 220, (*c*) dark-field second-order 440, critical voltage, and (*d*) as *c* in another region. Notice reduction in oscillatory contrast in *c* and *d*, indicating lengthened extinction distance, also high contrast but wider images in *d*.

which compares dislocation images in bright field, first-order dark field, and second-order dark field (critical voltage). Since the image width of dislocations is proportional to the extinction distance, ξg at V_c images tends to be broad (Fig. 15*d*) {since at V_c, ξg approaches infinity, see, e.g., ref. 22}. The contrast is very good since the background is low.

Many more applications of the critical voltage effect are needed. Although electron microscopes with energies >1 MeV permit a wider range of critical voltage to be measured, limitations are imposed if V_c is greater than the threshold energy for knock-on damage, since the latter may also affect the values of V_c.

POSSIBLE FUTURE TRENDS

The following is a suggested list of some future needs and possible trends in HVTEM:

1a. Improved reliability of 1 MeV microscopes.
 b. Increasing voltage to 1.5 MeV.
2. More research on contrast for complex solids, e.g., minerals.
3. Image processing and analysis.
4. Environmental chambers for a wide range of applications in biology and materials science (see Chapter 16).
5. More studies of radiation damage and resolution in organic (biological) solids (see Chapter 12).

6. More research on thick (biological) sections and stereomicroscopy.
7. Further applications of critical voltage.
8. Energy filtering analysis.
9. Three to 5 MeV instruments.

In addition to transmission microscopes, high-voltage scanning electron microscopy appears to be very promising (see Chapters 2 and 3), but there is a big question mark concerning the maximum voltage that seems desirable. For direct observations of knock-on radiation damage in crystals, transmission microscopes up to 1.5 MeV appear to be adequate; but for routine work in materials science and engineering 1 MeV seems to be optimum because of the limitations of knock-on damage. As far as ionization damage and ultimate resolution is concerned, it may be that 3 to 5 MeV is desirable, especially for studies of biological and polymeric materials. More experimental and theoretical work is urgently needed in this regard.

More interdisciplinary research will certainly come out of the HVEM area facilities, and we expect greater emphasis in mineralogy (although the advantages of HVEM are slow to be recognized by many mineralogists), process metallurgy, and applications to the characterization of a greater range of materials both organic and inorganic.

ACKNOWLEDGMENTS

I am grateful to the U.S.A.E.C. through the Inorganic Materials Research Division, Lawrence Berkeley Laboratory, for continued financial support of our programs. I wish to thank my students for providing me with examples of their research results.

REFERENCES

1. W. L. Bell and G. Thomas, *Electron Microscopy and Structure of Materials* (G. Thomas et al., ed.), Univ. California Press, Berkeley, 1972, p. 23.
2. G. Thomas, *Proceedings Third International Conference on High Voltage Electron Microscopy, Oxford*, Academic Press, London and New York, 1973.
3. G. Thomas, *Proceedings of Erice School on Electron Microscopy, Erice, Italy*, In press. (Valdré, ed.)
4. G. Thomas, *Proceedings of the 31st Annual Meeting of the Electron Microscopy Society of America* (C. J. Arceneaux, ed.), Claitors, Baton Rouge, 1973, p. 2.
5. G. Thomas, *Phil. Mag.*, **17,** 1097 (1968).
6. G. Thomas and J.-C. Lacaze, *J. Microscopy*, **97,** 301 (1973).
7. D. J. Barber, *J. Mater. Sci.*, **5,** 3 (1970).
8. L. C. De Jonghe and G. Thomas, *J. Appl. Phys.*, **41,** 4884 (1970).
9. L. C. De Jonghe and G. Thomas, *J. Mater. Sci., Eng* , **8,** 259 (1971).
10. J. Hornstra, *J. Phys. Chem. Solids*, **15,** 311 (1960).
11. M. H. Lewis, *Phil. Mag.*, **17,** 481 (1968).
12. O. van der Biest, Ph.D. Thesis, Univ. Calif., Berkeley, In progress: *Proceedings of the 31 Annual Meeting of the Electron Microscopy Society of America* (C. J. Arceneaux, ed.), Claitors, Baton Rouge, 1973, p. 24.
13. L. C. De Jonghe, Ph.D. Thesis, Univ. of Calif., Berkeley, UCRL Rep No. 20369, 1970; also 31st EMSA *Proceedings of the 31st Annual Meeting of the Electron Microscopy Society of America* (C. J. Arceneaux, ed.), Claitors, Baton Rouge, 1973, p. 26.

14. G. Ramaut, A. Lagasse, and S. Amelinckx, *Phys. Status Solidi*, **7**, 447 (1964).
15. M. von Heimendahl, G. Hubred, D. W. Fuerstenau, and G. Thomas, AEC Report LBL-1946, Lawrence Berkeley Lab., Berkeley, Calif., 1973.
16. G. Thomas, *Proceedings of the 28th Annual Meeting of the Electron Microscopy Society of America* (C. J. Arceneaux, ed.), Claitors, Baton Rouge, 1970, p. 2.
17. W. F. Müller, H. R. Wenk, W. L. Bell, and G. Thomas, *Contrib. Mineral Petrol.*, **40**, 63 (1973).
18. C. J. E. Kemster, H. D. Megaw, and E. W. Radoslorich, *Acta Cryst.*, **15**, 1005, 1017 (1962).
19. J. E. Wainwright and J. Starkey, *Z. Kristallogr* , **133**, 75 (1971).
20. J. M. Christie, J. A. Lally, A. H. Heuer, R. M. Fisher, D. T. Griggs, and D. V. Radcliffe, *Proceedings of the 2nd Lunar Conference on Geochemica and Cosmochimica Acta*, Vol. 1, Suppl. 2, 1971, p. 69.
21. A. H. Heuer, J. A. Lally, J. M. Christie, and S. V. Radcliffe, *Phil. Mag.*, **26**, 465 (1972).
22. M. J. Goringe, E. A. Hewat, C. J. Humphries, and G. Thomas, *Proceedings of the 5th International Congress on Electron Microscopy*, Inst. Physics, London, 1972, p. 538.
23. L. J. Chen, Ph.D. Thesis, Univ. California, Berkeley, In progress.
24. W. L. Bell, *Proceedings of the 7th International Congress of Electron Microscopy* (P. Favard, ed.), Soc. France de Mic. Elect. Paris, 1970, p. 81.
25. I. L. F. Ray and D. J. H. Cockayne, *Phil. Mag.*, **22**, 853 (1970).
26. J. S. Lally, C. J. Humphries, A. J. Metherell, and R. M. Fisher, *Phil. Mag.*, **25**, 321 (1972).
27. E. P. Butler, *Ibid* , *26*, 33 (1972).
28. W. L. Bell, *Proceedings of the 29th Annual Meeting of the Electron Microscopy Society of America* (C. J. Arceneaux, ed.), Claitors, Baton Rouge, 1971, p. 184.
29. E. P. Butler, *Phys. Status Solidi*, **18**, 71 (1973).

LEGAL NOTICE

This report was prepared as an account of work sponsored by the United States Government. Neither the United States nor the United States Energy Research and Development Administration, nor any of their employees, nor any of their contractors, subcontractors, or their employees, makes any warranty, express or implied, or assumes any legal liability or responsibility for the accuracy, completeness or usefulness of any information, apparatus, product or process disclosed, or represents that its use would not infringe privately owned rights.

TECHNICAL INFORMATION DIVISION
LAWRENCE BERKELEY LABORATORY
UNIVERSITY OF CALIFORNIA
BERKELEY, CALIFORNIA 94720